Plasma Sources
Science and
Technology

PAPER

Fast gas heating and peculiarities of temperature measurements by optical emission spectroscopy in nanosecond surface dielectric barrier discharge

To cite this article: Bin Zhang *et al* 2025 *Plasma Sources Sci. Technol.* **34** 095010

IOP Publishing Plasma Sources Science and Technology
Plasma Sources Sci. Technol. **34** (2025) 095010 (16pp) https://doi.org/10.1088/1361-6595/ae00ef

Fast gas heating and peculiarities of temperature measurements by optical emission spectroscopy in nanosecond surface dielectric barrier discharge

Bin Zhang[1,3], **Geoffrey Kreyder**[3,*], **Nikolay Popov**[2], **Sergey A Shcherbanev**[3] **and Svetlana M Starikovskaia**[3,*]

[1] College of Automation Engineering, Nanjing University of Aeronautics and Astronautics, Nanjing 211106, People's Republic of China
[2] Skobeltsyn Institute of Nuclear Physics, Moscow State University, Leninsky gory, Moscow 119991, Russia
[3] Laboratory of Plasma Physics (CNRS, Ecole Polytechnique, Univ. Paris-Sud, Observatoire de Paris, Sorbonne Université, l'Institut Polytechnique de Paris), Ecole Polytechnique, route de Saclay, 91128 Palaiseau, France

E-mail: geoffrey.kreyder@lpp.polytechnique.fr and svetlana.starikovskaia@lpp.polytechnique.fr

Received 17 June 2025, revised 5 August 2025
Accepted for publication 29 August 2025
Published 23 September 2025

Abstract

The aim of this work is the experimental and theoretical study of nanosecond Surface dielectric barrier discharge (SDBD) parameters in atmospheric pressure air. Measurements of electric current and delivered energy, ICCD images of the discharge at all stages of its evolution, and gas heating in the discharge and near afterglow are performed. The paper presents the results of 2D numerical modeling of the nanosecond SDBD. The results of the calculations are compared with measured data on the dynamics of current, energy input and gas heating. Special attention is paid to the study of the spatial structure of the discharge, in particular, to the distribution of gas temperature and the second positive system emission intensity in the direction perpendicular to the surface of the dielectric. It is shown that the results of temperature measurements in SDBD using optical emission spectroscopy technique are severely influenced by this spatial structure. The parameters of a probe discharge of smaller amplitude, which is formed by a reflected pulse 500 ns after the main discharge, are also calculated. The possibility of using the second diagnostic pulse to measure the gas temperature in the afterglow discharge is discussed.

Keywords: nanosecond SDBD, temperature measurements from rotational lines, numerical modeling of nSDBD, fast gas heating, energy efficiency

1. Introduction

Surface dielectric barrier discharge (SDBD) has been extensively studied in recent years due to its potential applications in the field of aerodynamics [1–4]. In an SDBD setup, the electrodes are typically arranged in a planar configuration, with a powered electrode placed directly on the surface of a dielectric layer and a ground electrode placed on the opposite side beneath the dielectric. This configuration is traditionally called 'airflow' or 'actuator' design of the SDBD [5]. At atmospheric pressure, microdischarges appear in the vicinity of the high-voltage electrode and develop into streamers propagating along the dielectric surface; in nanosecond SDBDs, the start

* Authors to whom any correspondence should be addressed.

of the streamers from the edge of the high-voltage electrode is synchronous with the accuracy of at least 0.2 ns [6]. Studies of fast gas heating (FGH) in SDBDs are of particular interest, since this effect can be important for plasma actuators [7, 8].

FGH is an abrupt increase in gas temperature in non-equilibrium low-temperature plasma due to relaxation of electronically excited states of atoms and molecules [9]. The observed heating can be as high as thousands of kelvins during tens of nanoseconds at atmospheric pressure [10]. In the flow control, FGH is responsible for thermal frequency perturbations in the range of unstable frequencies of flow instabilities. Experimental studies of FGH in pulsed nanosecond discharges have been carried out under various conditions, over a wide range of reduced electric field $E/N = 90 - 400$ Td. Atmospheric pressure discharges [10–13], medium and reduced pressure discharges, namely $P = 100$ Torr [14], $P = 27$ mbar [15], $P = 3 - 10$ mbar [16] at different specific delivered energy (SED) were investigated. Measurements of gas temperature in nanosecond discharges are often based on analysing the population of rotational levels of $N_2(C^3\Pi_u, v)$ by measuring the emission of the second positive system, $N_2(C^3\Pi_u) \rightarrow N_2(B^3\Pi_g)$. Less commonly, spontaneous Raman scattering [12, 13], and picosecond CARS spectroscopy [14] are used to measure the gas temperature.

According to [9, 17], the existing theoretical models describe most of the available experimental data on FGH in the field range $E/N \leqslant 500$ Td. At higher fields, studies of FGH have been carried out in [6, 18–20]. In these works, a SDBD was ignited in atmospheric pressure air, the pulse duration was 25 ns, and the applied voltage on a high-voltage electrode $U \leqslant 42$ kV. In addition, in [20] FGH was studied in N_2:O_2 mixtures at different oxygen fractions, 0%–50%, for the pressure range $P = 450 - 760$ Torr. The gas temperature was measured on the basis of the rotational spectrum of the second positive system of molecular nitrogen [21, 22]. The spectra were integrated over the pulse and measured in the discharge and in the near afterglow, at 1 μs. To excite the gas 1 μs after the main discharge, a reflected pulse was used, the amplitude of the probe pulse being approximately 5 times smaller than the amplitude of the main pulse. The part of energy spent on FGH, η_R, was found to be only slightly changed with the applied voltage and the gas pressure. It was reported that η_R significantly increases after the discharge pulse: for example, at $U = +41$ kV on the high voltage electrode (+20.5 kV pulse amplitude from the generator) in air at 600 Torr the part of energy spent on the FGH immediately after discharge is $\eta_R \sim$15%–20%, and at 1 μs after the discharge $\eta_R > 60\%$ (see figure 5 of [20]).

Optical emission was used to measure gas temperature in atmospheric pressure nanosecond SDBD in [23, 24]. The spectra were taken at $U = \pm 45$ kV on the electrode with 1 ns time resolution and 1 mm space resolution. It was shown that during the first few nanoseconds, gas heating of 70–80 K is observed. According to estimates [23], the average specific deposited energy near the high-voltage electrode comprised $\omega = 0.1$ eV/-molecule, providing the efficiency of the FGH η_R =15%–17%.

Fast heat release in reactions involving charged and electronically excited species has been analyzed for an atmospheric-pressure nanosecond SDBD [25] using 2D numerical modeling with the help of PASSKEy code [26]. The model was based on the direct coupling of a self-consistent fluid model with detailed kinetics, photoionization and Euler equations. The reduced electric field and the electron density were examined for $U = \pm 24$ kV voltage pulses on a high-voltage electrode. The main processes contributing to the FGH in nanosecond SDBD were quantitatively analysed. The distribution of FGH energy over the processes was compared with findings in the literature.

The studies discussed above were conducted in single-shot mode or at low pulse repetition frequencies, typically on the order of a few Hz. In addition, nanosecond repetitively pulsed SDBDs have also attracted attention [7, 27]. A key focus of the review [7] is the dynamics and kinetics of near-surface discharge plasmas in SDBD systems driven by AC and repetitively pulsed waveforms. Particular attention is given to diffuse and contracted discharge modes. It is shown that the use of alternating polarity pulse waveforms accelerates the contraction of SDBDs and promotes the formation of filamentary plasmas.

The aim of this work is the experimental and theoretical study of the parameters of the nanosecond SDBD in atmospheric pressure air. Measurements of electric current and delivered energy, ICCD images of the discharge at all stages of its evolution, and gas heating in the discharge and near afterglow are performed. The paper presents the results of 2D numerical modeling of the nanosecond SDBD. The results of the calculations are compared with measured data on the dynamics of discharge current, delivered energy and gas heating. The peculiarities of gas temperature measurements by optical emission spectroscopy in nanosecond SDBD are discussed.

2. Experimental setup

SDBD discharge was studied in a classical airflow configuration. The electrode system is schematically shown in figure 1(a). High-voltage and low-voltage electrodes made of 0.1 mm thick copper foil were glued to different sides of a 0.5 mm thick PVC layer. The dimension of the high-voltage ABCD and low-voltage DCFE electrodes are indicated in the caption of figure 1(a). External edges of the high-voltage electrode (DA, AB and BC) were protected by an additional dielectric layer to avoid parasitic discharges. The waveform of the voltage pulse on the high-voltage electrode used in this paper is given by figure 1(b).

Figure 2 provides a schematic of the experimental setup. High-voltage pulses were delivered from the high voltage generator FDS 3–1NM1 (FID) to the electrodes by 50 m long coaxial cable. The central wire of the cable was connected to the high-voltage electrode, while the shielding was connected to the low-voltage electrode. In this configuration, the SDBD cell acted as the terminal load of the coaxial cable. The high-voltage cable connection to the electrodes was thoroughly insulated, the absence of electrical

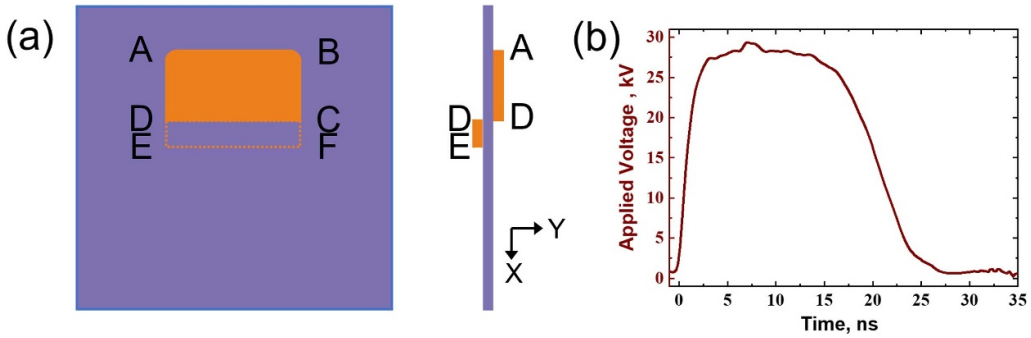

Figure 1. (a) The scheme of the electrode system. $|AB| = |DC| = |EF| = 25$ mm; $|AD| = |BC| = 10$ mm; $|CF| = |DE| = 6$ mm; (b) a typical waveform of the high voltage on the electrode. Orange color is for copper, violet is for PVC.

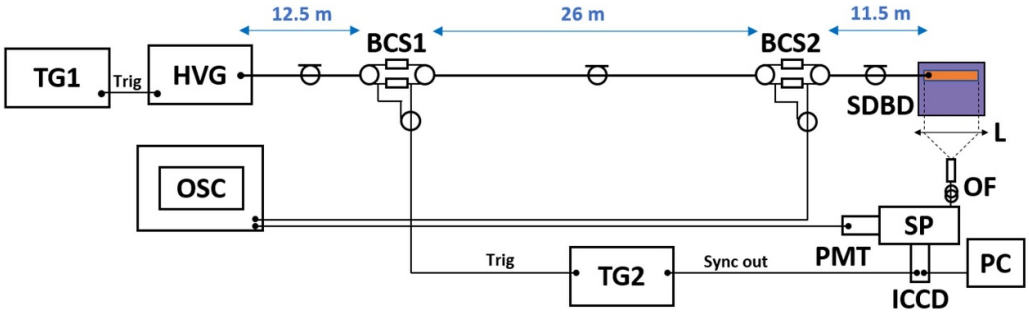

Figure 2. Experimental setup for the measurement of the optical emission spectroscopy illustrating the following equipments. HVG: high voltage generator, TG: triggering generator, SDBD: Surface Dielectric Barrier Discharge, OSC: oscilloscope, BCS: back-current shunt, L: lens, OF: optical fiber, SP: spectrometer, PMT: photomultiplier Tube, ICCD: ICCD-camera, PC: personal computer.

leakage or parasitic discharges was checked with ICCD imaging. The key parameters of the voltage pulse at the high-voltage electrode were as follows: rise time of 4 ns, pulse duration at FWHM of 20 ns, and a voltage amplitude $U = +27.5$ kV.

To measure the current and energy delivered to the plasma, a custom-calibrated back current shunt (BCS2) was soldered into the shielding of the high-voltage cable at a distance of 11.5 m from the discharge cell. Additional BCS unit (BCS1) was placed at 12.5 m from the high-voltage generator (HVG) and used for triggering. The attenuated signal from BCS2 was recorded using a Tektronix DPO5104B oscilloscope. The energy due to charging of the electrode capacitance and the attenuation in the cable were taken into account. The electrical current through the discharge was calculated as the difference between the pulses incident and reflected from the discharge cell. The energy was determined from the difference between energies of incident and reflected pulses. The details of the technique concerning the advantages of long coaxial cables and back current shunts can be found elsewhere [28–30].

Spectrally integrated plasma images (200–800 nm) were captured by ICCD camera (PIMax4, Princeton Instruments) equipped with a Canon TV Zoom lens (TV 6X18). The emission of atmospheric pressure SDBD in UV–vis in air corresponds mainly to the $N_2(C^3\Pi_u) \rightarrow N_2(B^3\Pi_g)$ transition (the second positive system of molecular nitrogen, SPS) [31]. The quenching time of the excited levels is determined by the collision of excited nitrogen molecules with molecular oxygen, the rate constant being equal [32] to $2.7 \cdot 10^{-10}$ cm^3 s^{-1}. The efficient lifetime of $N_2(C^3\Pi_u)$ is 0.7 ns at atmospheric pressure. So the emission reflects instantaneous excitation of $N_2(C^3\Pi_u)$ by electron impact: $e + N_2(X^1\Sigma_g^+) \rightarrow e + N_2(C^3\Pi_u)$, and the resolution is limited by the camera gate. A series of high-resolution images was also taken with a long-distance microscope (LDM-1UV, LaVision), achieving a spatial resolution of 7.2 μm·pixel^{-1}.

To take optical emission spectrum, the diaphragm was installed in the vicinity of the discharge so that it allowed emission from the region 0 to 2 mm from the edge of the high voltage electrode. The emission was collected by the optical fiber and delivered to the entrance of the Acton SP2500 spectrometer (Princeton Instruments, 1200 ln·mm^{-1} grating) coupled with the ICCD PI-Max4 camera. A spectral transmission function was calibrated using a Hg/Ar lamp (Princeton Instruments).

The optical emission spectra of the $N_2(C^3\Pi_u) \rightarrow N_2(B^3\Pi_g)$ transition were used to measure the rotational temperature in the pulse and in the afterglow. The modeling of the spectra was performed using the SpecAir code [22]. The spectra were recorded using a 1 ns ICCD gate at the rising and trailing edges of the initial pulse. To measure the temperature in the afterglow, a probe pulse of lower amplitude arriving at the high-voltage electrode with 500 ns delay, was used. After the primary pulse reached the electrode, most of the energy is

reflected and travels back along the cable. Due to the design of the FID generator, this reflected pulse decreases significantly by 80% in amplitude, then travels back to the electrode as a probe pulse with an amplitude of approximately 5.2 kV. This probe pulse was sufficient to re-ignite the discharge and provide the $N_2(C^3\Pi_u)$ emission, although less intense than in the first pulse. The ICCD gate for the probe pulse was equal to 40 ns. The absence of optical emission of the second positive system before the probe pulse was verified.

3. Model description

As noted previously, SDBD consists of a system of plasma channels that propagate from the high-voltage electrode along the dielectric surface. Numerical modeling of these channels is a three-dimensional, time-dependent problem in which all discharge plasma parameters exhibit significant spatial and temporal variations. Currently, there is no comprehensive quantitative description of SDBD parameters within the framework of a full-scale 3D model. In most studies, SDBD modeling relies on a two-dimensional approximation, which accounts for plasma inhomogeneity in the direction of discharge propagation and perpendicular to the dielectric surface, while assuming homogeneity in the third direction [25, 26, 33, 34]. As a result, the evolution of a uniform plasma layer along the dielectric surface is considered, while the transverse structure of the discharge is neglected.

To follow the FGH dynamics and to obtain a deep insight into the measurements of gas temperature in SDBDs, a 2D computational framework is designed with PASSKEy (PArallel Streamer Solver with KinEtics) code, which has been used and validated in nanosecond surface discharges [25, 26, 35, 36], pin-to-pin discharges [37], pin-to-plane discharges [38], capillary discharges [39], and other works investigating short pulsed discharges [40–43]. Detailed mathematical formulations and the strategy for multiphysics and multiscale coupling can be found elsewhere [26, 42, 44, 45]. Here, only a brief introduction to the solved equations is presented below.

3.1. Equations for plasma module

The drift-diffusion reaction equation for species is:

$$\frac{\partial n_i}{\partial t} + \nabla\cdot\boldsymbol{\Gamma_i} + \nabla\cdot(n_i\cdot\boldsymbol{u_g}) + \nabla\cdot(D_i\nabla n_i) = S_i + S_{\rm ph}, i = 1,2,\ldots,N_{\rm total} \quad (1)$$

n_i is the number density for each species i. S_i represents the source term of the species i, calculated based on detailed reaction kinetics. The kinetic scheme of our previous paper [37] is used here, which effectively describes the streamer dynamics and the FGH process in the air. The scheme includes in total 24 species and 92 reactions. Following neutral, charged, excited species are taken into account: e, N_2, N_2^+, N^+, N_4^+, $N_2(A^3\Sigma_u^+)$, $N_2(B^3\Pi_g)$, $N_2(a'^1\Sigma_u^-)$, $N_2(C^3\Pi_u)$, N, N(^{2}D), N(^{2}P), O_2, O, O(^{1}D), O(^{1}S), O_2^+, O^+, O_4^+, O^-, O_2^-.

The term S_{ph} represents the source of photoionization and is determined by three-exponential Helmholtz equations. The flux for species i is:

$$\boldsymbol{\Gamma_i} = (q_i/|q_i|)\,\mu_i n_i \boldsymbol{E} - D_i\nabla n_i, i = 1,2,\ldots,N_{\rm ch} \quad (2)$$

where q_i, μ_i and D_i are the number density, charge, flux, mobility, and diffusion coefficients for each species i, respectively. $\boldsymbol{E}$ is the electric field.

The electron energy equation for mean electron energy is given as:

$$\frac{\partial}{\partial t}(n_e\epsilon_m) + \nabla\cdot\boldsymbol{\Gamma_\epsilon} + \nabla\cdot(n_e\epsilon_m\cdot\boldsymbol{u_g}) = -|q_e|\cdot\boldsymbol{\Gamma_e}\cdot\boldsymbol{E} - P(\epsilon_m) \quad (3)$$

$$\boldsymbol{\Gamma_\epsilon} = -n_e\epsilon_m\mu_\epsilon\boldsymbol{E} - D_\epsilon\nabla(n_e\epsilon_m) \quad (4)$$

where ϵ_m, μ_ϵ, D_ϵ are mean electron energy, electron energy mobility, and diffusion coefficient, respectively. $P(\epsilon_m)$ represents the power lost by electrons in collisions. The local mean energy approximation (LMEA) is employed in this work, whereby the rate coefficients for electron-impact reactions, electron transport (swarm) parameters, and the power loss by electrons are assumed to depend solely on the local mean electron energy, ϵ_m. These dependencies are determined by solving the Boltzmann equation in the two-term approximation using the BOLSIG+ solver [46]. The relevant quantities are precomputed as functions of ϵ_m, tabulated, and subsequently interpolated during simulations based on the locally calculated ϵ_m.

In equations (1) and (3), three correction terms are considered in the governing equations to account for the coupling between plasma and fluid. $\nabla\cdot(n_i\cdot\boldsymbol{u_g})$ and $\nabla\cdot(n_e\epsilon_m\cdot\boldsymbol{u_g})$ represent the convection terms of plasma species and electron energy, respectively, induced by gas flow. $\nabla\cdot(D_i\nabla n_i)$ represents the diffusion term of the species.

The electric field is determined by solving the Poisson equation coupled with space charge:

$$\nabla(\varepsilon_0\varepsilon_r(-\nabla\Phi)) = -\rho_q - \rho_c \quad (5)$$

$$\boldsymbol{E} = -\nabla\Phi \quad (6)$$

$$\rho_q = \sum_{i=1}^{N_{ch}} n_i q_i \quad (7)$$

$$\frac{\partial\rho_c}{\partial t} = \sum_{i=1}^{N_{ch}} q_i(-\nabla\cdot\boldsymbol{\Gamma_i}) \quad (8)$$

where ε_0 and ε_r are the vacuum permittivity and relative permittivity, respectively. Φ is the electric potential, ρ_q is the space charge, and ρ_c is the surface charge determined by the flux of ions at the interfaces between the plasma and the dielectric.

3.2. Equations for fluid module

The Fluid Module solves the two-dimensional Navier–Stokes equations, which are expressed in the following form:

$$\frac{\partial \boldsymbol{U}}{\partial t}+\frac{\partial \boldsymbol{F}}{\partial x}+\frac{\partial \boldsymbol{G}}{\partial y}=\boldsymbol{S} \tag{9}$$

$$\boldsymbol{U}=\begin{bmatrix}\rho\\ \rho u\\ \rho v\\ \rho E\end{bmatrix},\boldsymbol{F}=\begin{bmatrix}\rho u\\ \rho u^2+p-\tau_{xx}\\ \rho uv-\tau_{xy}\\ (\rho E+p)u-k\frac{\partial T}{\partial x}-u\tau_{xx}-v\tau_{xy}\end{bmatrix} \tag{10}$$

$$\boldsymbol{G}=\begin{bmatrix}\rho v\\ \rho uv-\tau_{yx}\\ \rho v^2+p-\tau_{yy}\\ (\rho E+p)v-k\frac{\partial T}{\partial y}-u\tau_{yx}-v\tau_{yy}\end{bmatrix},\boldsymbol{S}=\begin{bmatrix}0\\ q_i n_i E_x\\ q_i n_i E_y\\ Q_g\end{bmatrix} \tag{11}$$

where ρ represents the mass density, p is the gas pressure, u and v are the velocity components, ρE is the total energy density, k is the thermal conductivity, T denotes the gas temperature. τ_{xx}, τ_{xy}, τ_{yx}, and τ_{yy} are viscous stress components.

$q_i n_i \boldsymbol{E}$ represents the electric force generated by the net charge. Q_g is the heat source term, calculated as the sum of the gas energy changes caused by reactions (inelastic collisions) between heavy particles:

$$Q_g=\sum_j R_j \Delta E_j \tag{12}$$

where R_j and E_j are the reaction rate and the energy release of the reaction j, respectively.

3.3. Geometry, initial and boundary conditions

The SDBD electrode configuration, with a computational domain of 3 cm × 3 cm, is shown in figure 3, which is extracted from the experiment. The simulated initial condition is 1 atm pressure and 300 K. A uniform mesh size of 2 μm is assigned for the plasma domain, beyond the plasma domain the mesh size grows exponentially until the end of the entire computational domain.

The initial electron density is $n_{e0}=10^4$ cm^{-3} uniformly distributed in the plasma region, and the ion density is given based on quasi-neutrality. The initial mean electron energy is set as 0.5 eV. The details of the boundary conditions of transport equations, Poisson's equation and Helmholtz equations are described in [42, 45]. 2D maps of calculated plasma parameters are presented in the appendix A and will be discussed below.

For additional validation of the model, calculations of the FGH in SDBD were performed for the experimental conditions [23, 24] (pulse duration = 20 ns, applied voltage on the electrode of positive polarity $U=45$ kV). The results of comparison of the calculated results and experimental data are given in the appendix B.

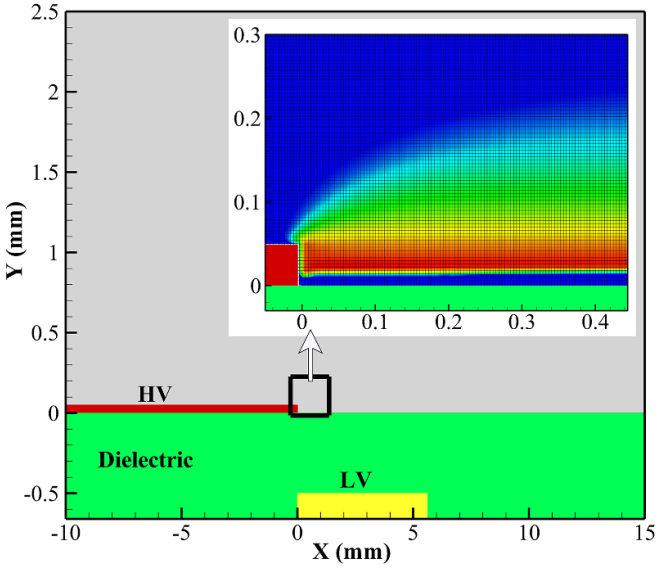

Figure 3. The geometry and mesh distribution. High-voltage electrode: red domain; dielectric: green domain; grounded low-voltage electrodes: yellow domain.

4. Results and discussion

4.1. Experimental results

Nanosecond SDBDs have been experimentally studied in two configurations: when the grounded electrode is much longer than the maximum length of streamer propagation $L_{\max}$ [24, 26], and when the grounded electrode is comparable to or shorter [6, 47] than $L_{\max}$. The first configuration is preferred as a base case for fundamental studies and comparison with numerical simulations, when the grounded electrode is considered infinite in the direction perpendicular to the edge of the high-voltage electrode [26]. The second case is of interest when a more localized plasma is required, or when in numerical modeling the accent is made on a few first millimetres of the discharge propagation [34, 48]. It is important to note that at the first few nanoseconds of the voltage pulse applied to the electrodes the SDBD in both configurations is rather similar.

Figure 4 compares the ICCD images of the positive polarity discharge in 1 atm surrounding air in these two configurations: 60 mm low-voltage electrode for (a)–(d) [24], and $|DE|=6$ mm low voltage electrode for (e) and (f) of the present work. The optical emission corresponds to the second positive system of molecular nitrogen.

The character of the discharge development is similar: for both configurations, rapid (5–7 mm ns^{-1}) synchronous propagation of streamers is observed from the edge of the high-voltage electrode at the leading edge of the pulse, then the absence of radiation, and then, at the trailing edge of the pulse, a second radiation front is observed, slower (around 1 mm ns^{-1}), also moving from the edge of the high-voltage electrode. The 'side view' images ((c), (d)) provide a characteristic diameter of a streamer: 150–200 μm. Will note that in the case of a 60 mm low-voltage electrode, after 5 ns the discharge continues to spread and the streamers travel 25–30 mm

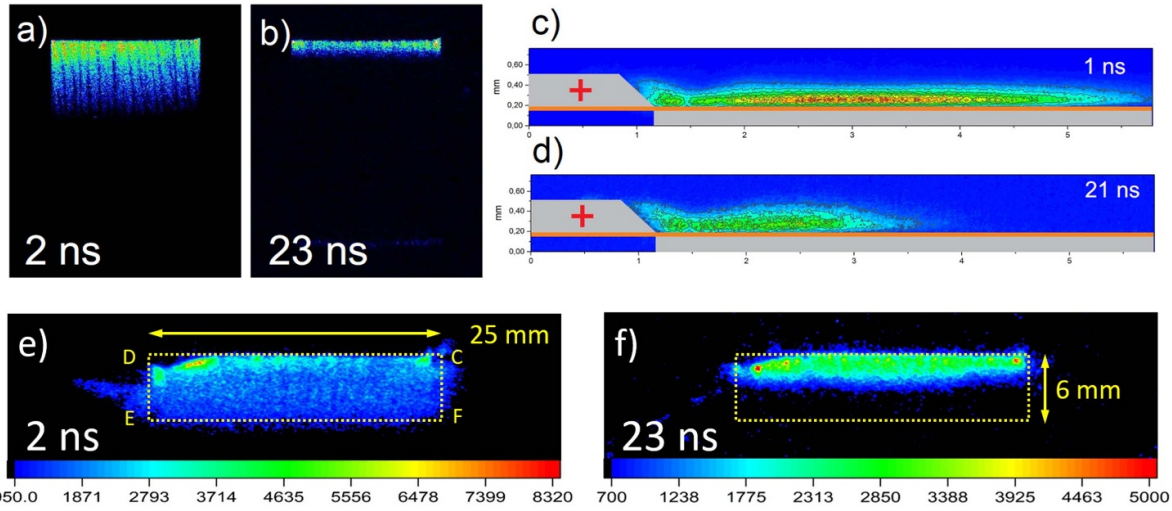

Figure 4. General ICCD images of SDBD discharges with ICCD gate equal to 1 ns. Numbers in each frame mean the time delay from the beginning of the discharge. (a), (b), (c), (d) — similar geometry with longer grounded electrode ($|DE| = 60$ mm) [24]; (e), (f) — ICCD images of the discharge in the setup corresponding to this paper, $|DE| = 6$ mm.

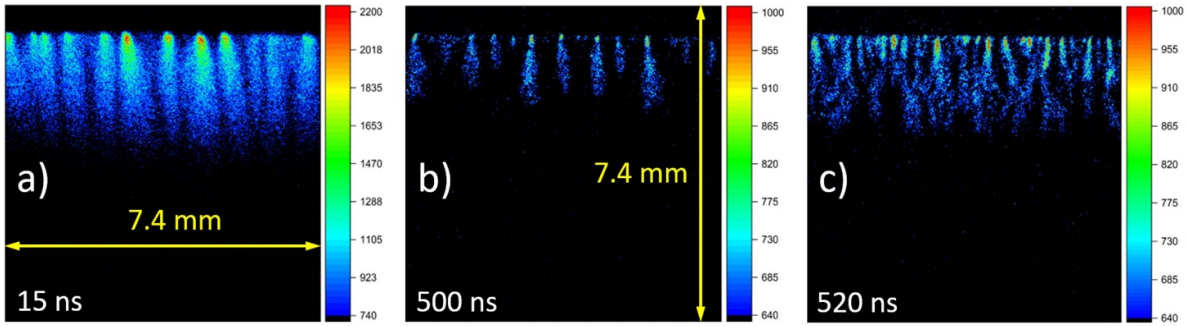

Figure 5. Zoomed ICCD-images of streamers starting from the edge of the high-voltage electrode taken with the help of the long distance microscope. Gate 10 ns. (a) — trailing edge of the main pulse, (b) — rising front of the probe pulse, (c) — trailing edge of the probe pulse. Numbers in each frame mean the time delay from the beginning of the discharge.

during a 20 ns pulse [26], while in the case of a $|DE| = 6$ mm low-voltage electrode the plasma remains 'confined' above the low-voltage electrode, without further spreading.

In addition, taken through the long distance microscope zoomed ICCD images show more detailed structure of the surface streamers. The trailing edge of the main pulse (figure 5(a)) and the probe pulse (figures 5(b) and (c)) images are compared. The rising front of the probe pulse (figure 5(b)) is quite similar to the main (first) pulse: the same number of streamers is observed, although the streamers seem to be less similar to each other in length for a given time instant. The trailing edge of the probe pulse (figure 5(c)) shows different structure: a typical diameter of streamers is smaller; their density per unit length of the edge of the high-voltage electrode seems to be higher.

Experimentally measured power and total energy deposited in plasma are given by figure 6. The energy increases monotonically, reaching the value of 11.1 mJ at 19 ns. At the trailing edge of the pulse, the energy increases again and reaches $W \approx 12.7$ mJ. The power waveform presented in the same figure shows that the maximum power is deposited to plasma in relatively high fields near the discharge front, but the deposited energy increases monotonically and, as a result, most of energy is deposited after the front, where the fields are significantly lower.

Synchronized waveforms of emission of the second positive system, electric current and voltage on the high-voltage electrode are given by figure 7. A good correlation between the time behavior of emission measured by ICCD and by photomultiplier is observed. Two separate peaks of emission are observed. For both rising front and trailing edge, the FWHM of the emission pulse is twice shorter than the FWHM of the corresponding peak of the electric current, comprising 2 ns/4 ns at the rising front and 5 ns/10 ns at the trailing edge respectively.

Both emission peaks were used to measure the rotational temperature. An additional measurement was performed in the probe pulse, 500 ns after the main pulse. A long coaxial high-voltage cable ensured the absence of any electrical reflections and, accordingly, any disturbances on the high-voltage electrode between the main and the probe pulses, which was controlled by the back current shunts. Rotational spectra in the middle of the edge of the high–voltage electrode collected

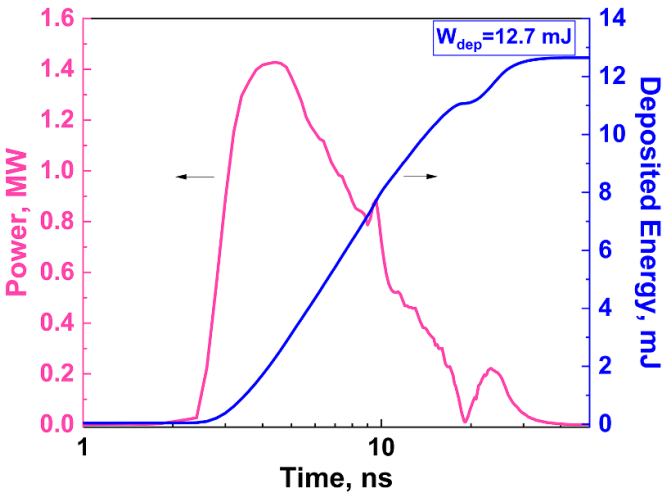

Figure 6. Experimentally measured power and energy deposited in plasma.

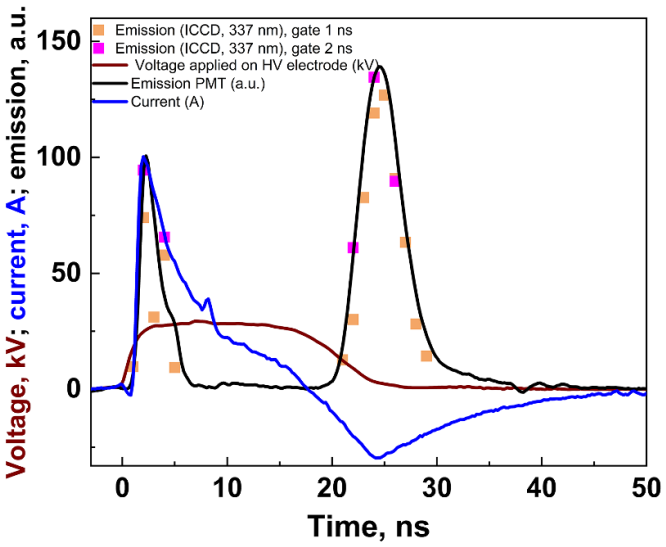

Figure 7. Experimentally measured by ICCD and by PMT waveforms of optical emission at $\lambda = 337.1$ nm superimposed with the electrical current and the voltage on the high-voltage electrode.

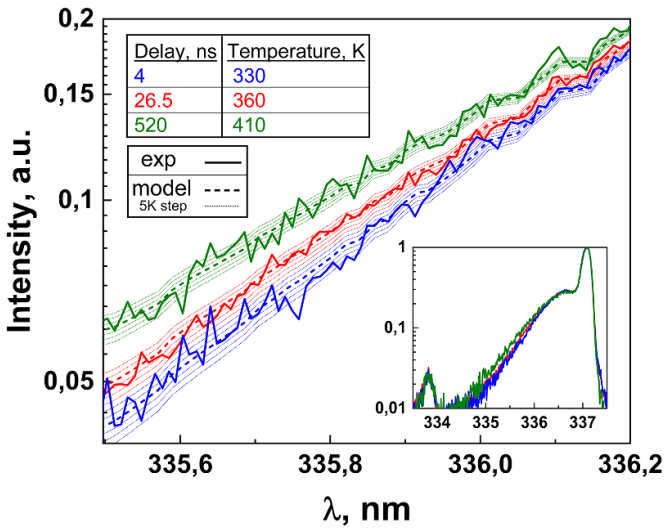

Figure 8. Distribution of emission in rotational spectra of N_2 at different time delays, 4 and 26.5 ns for the first pulse (ICCD gate is 1 ns) and 520 ns for the probe pulse (ICCD gate is 40 ns covering 500–540 ns time interval), and corresponding rotational temperatures. The insert shows the full-scale view of the spectra.

from $0-2$ mm distance from the electrode with the ICCD gate 1 ns, are presented in figure 8. Temperature uncertainties are ± 15 K. Short-dashed thin curves represent temperature increments of 5 K around the modeled temperature.

It should be noted that at high rotational numbers J, the rotational distribution of $N_2(C^3\Pi_u, v = 0, J)$ appears overpopulated. These 'hot' rotational states are distinctly visible in the spectra recorded at the trailing edge of the first main pulse. To ensure accurate fitting, these overpopulated regions were excluded from the spectral analysis. A possible origin of this 'hot' group is the electron-ion recombination of N_4^+ ions, $N_4^+ + e \rightarrow N_2(C^3\Pi_u) + N_2(X^1\Sigma_g^+)$ [49, 50], see the kinetic curves for N_4^+ and $N_2(C^3\Pi_u)$ discussed later (figures 11 and 16).

The most significant impact of these 'hot' states on the experimentally determined temperature was observed at the tail of the rotational distribution, corresponding to wavelengths $\lambda < 335$ nm. Consequently, this interval was deliberately excluded from consideration during data processing.

To relate a rotational temperature of the excited state, $T_{\rm rot}$ to a gas temperature T_g, the analysis of the $N_2(C^3\Pi_u)$ thermalization should be made [15, 21, 51], comparing the relative values of the RT–relaxation time ($\tau_{\rm RT}$) [52] and a characteristic time during which the excited species is produced or quenched. Under the conditions of the present work, the characteristic RT–relaxation time is $\tau_{\rm RT} = 0.4$ ns [52], and we accept $T_{\rm rot} = T_g$.

4.2. Results of numerical modeling

4.2.1. Discharge parameters in the first (main) pulse. Figure 9 shows the measured and the calculated temporal evolution of the discharge current together with the voltage pulse ($U = +27.5$ kV amplitude) on the high-voltage electrode. In numerical modeling, the current per unit length was calculated and multiplied by the electrode width ($|25|$ mm in the figure 1). Excellent agreement between measurements and calculations is clearly observed. Both the experiments and the simulations reveal two peaks in the electric current, corresponding to two distinct ionization waves appearing within the main (first) high-voltage pulse. The first ionization wave occurs at the rising front of the high voltage pulse, when the polarity of the high-voltage electrode is positive relative to the dielectric surface. During this period, the surface of the dielectric becomes positively charged. After $t > 15$ ns, the voltage on the high-voltage electrode begins to decrease, reversing the difference of potentials between the high-voltage electrode and the plasma. The high-voltage electrode then becomes negatively

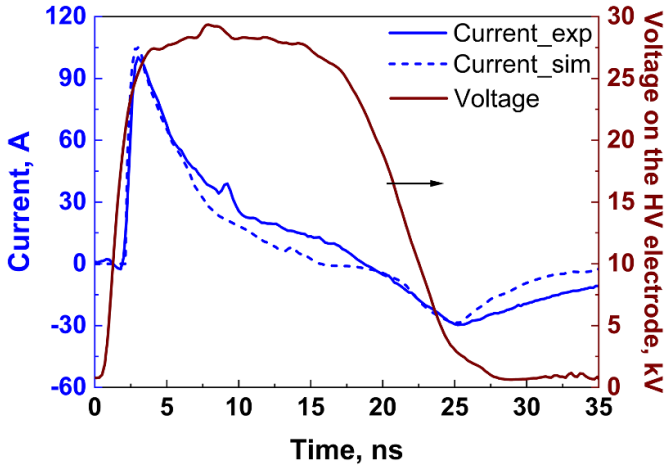

Figure 9. Waveforms of experimentally measured (solid line) and calculated (dashed line) electric current and the voltage pulse on the high voltage electrode in air, $P = 1$ atm. To compare the waveforms, calculated current density per unit length, [A cm^{-1}], was multiplied by a width of the high-voltage electrode $|AB|$.

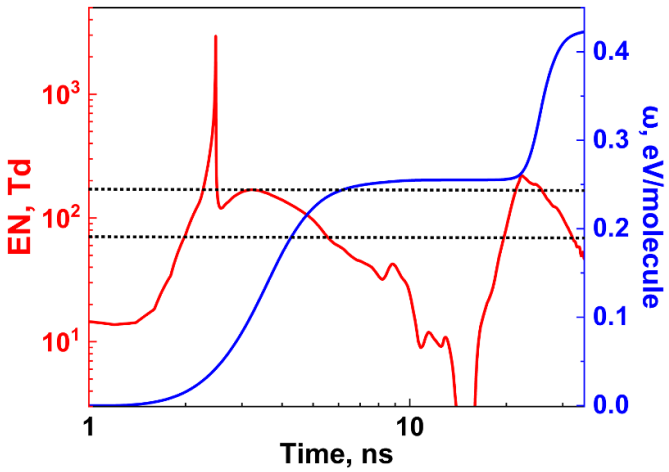

Figure 10. Temporal evolution of calculated reduced electric field E/N and specific delivered energy ω at the point $(x; y) = (1$ mm; 12.5 μm) for the conditions of figure 9.

charged relative to the positively charged dielectric surface. Consequently, another ionization wave, corresponding to the trailing edge of the main voltage pulse, propagates from the high voltage electrode of negative polarity. 2D maps of calculated electron density and reduced electric field in the first (main) pulse are given in appendix A. These two ionization waves can be clearly seen at 3 and 23–28 ns.

Calculated waveforms of the absolute value of the reduced electric field E/N and specific energy deposited in gas, SED, at the selected point over the dielectric are presented in figure 10. While the electric field at the head of the surface streamer reaches high values of $E/N =$ 1000–3000 Td, the majority of the discharge energy is deposited in the gas later, within a range of reduced electric fields of $E/N = 70$–170 Td (indicated by horizontal dashed lines in the figure). This field range is referred to as the effective reduced electric field, $(E/N)_{\text{eff}}$,

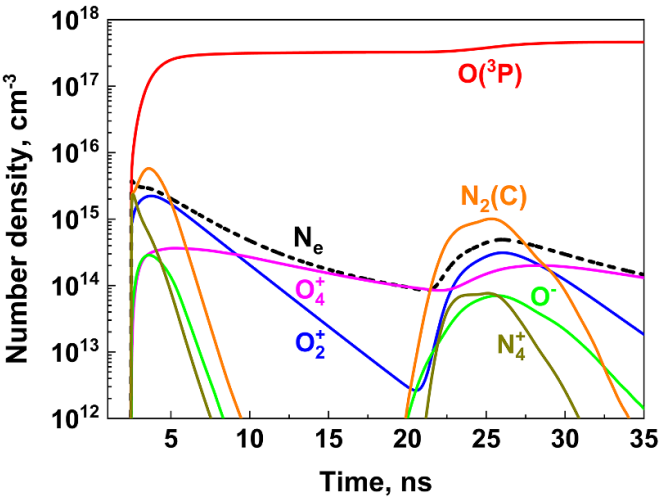

Figure 11. Time behavior of the electron density, density of ions and atomic oxygen at the point $(x; y) = (1$ mm; 12.5 μm) for the conditions of figure 9.

since it represents the conditions under which most of the energy transfer to the gas occurs. The peak electric fields is mainly responsible for ionization: the electron density reaches $N_e = 4 \cdot 10^{15}$ cm^{-3} at $t = 3.5$ ns (see figure 11), and this corresponds to the SED rise.

The fraction of discharge energy spent to the FGH, denoted as η_R, can be estimated using the data on the effective reduced electric field, $(E/N)_{\text{eff}}$. Based on experimental measurements [10–12, 53] and computational results [9, 17], at $E/N =$70–170 Td, the energy efficiency for FGH is $\eta_R =$ 6%–14%. Under these conditions, with a specific energy input of $\omega = 0.42$ eV/molecule, the expected gas temperature increase, ΔT, should be about 120–270 K.

Figure 11 shows the kinetic curves of atoms and charged particles calculated at a distance of 1 mm from the high-voltage electrode at 12.5 μm from the surface of the dielectric. The electron density decreases significantly (40–50 times) during the first 20 ns due to the electron–ion recombination with O_2^+ and O_4^+ ions. The decay of the emitting $N_2(C^3\Pi_u)$ state is even faster, demonstrating excellent agreement with experimental observation of the short emission and long current peaks for both the rising front and the trailing edge of the main pulse. The production of atomic oxygen is quite efficient, the concentration of atoms reaches $[O(^3P)] = 4 \cdot 10^{17}$ cm^{-3}. The density of negative ions is relatively low.

This work places special emphasis on analyzing the accuracy of temperature measurements based on the emission from the rotational bands of the second positive system of molecular nitrogen. This method is widely used to measure the gas temperature in SDBDs. Now we focus on the non-uniform gas temperature distribution along the OY axis, perpendicular to the dielectric surface, $T_g(y)$. The measured temperature T_m, depends not only on the actual temperature but also on the spatial distribution of SPS emission intensity, integrated over the detector's depth of field (DOF). Assuming the DOF is comparable to or larger than the streamer diameter (approximately

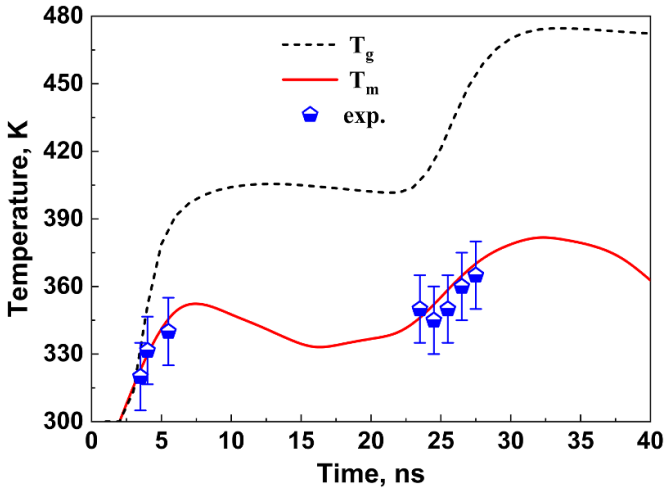

Figure 12. Temperature as a function of time in the main pulse: symbols are experimental data, curves are the results of calculations: dashed curve represents calculated gas temperature $T_g(t)$ at the point $(x; y) = (1$ mm; 12.5 μm), solid curve provides $T_m(t)$ calculated by equation (13) (see text) at $x = 1$ mm.

0.2 mm at atmospheric pressure), the expression for the expected to be measured temperature T_m is as follows [15]:

$$\frac{1}{T_m} = \frac{\int_0^L [\mathrm{N_2(C)}]/T_g \, \mathrm{d}y}{\int_0^L [\mathrm{N_2(C)}] \, \mathrm{d}y}, \qquad (13)$$

where $[\mathrm{N_2(C)}]$ is a density of $\mathrm{N_2(C^3\Pi_u)}$-state, and L is the thickness of the plasma region in the OY direction.

Figure 12 presents the calculated gas temperature for two cases: (i) T_g is the gas temperature at the point $(x; y) = (1$ mm; 12.5 μm); (ii) T_m is the expected to be measured temperature over the depth of field (DOF) at $x = 1$ mm, provided by the equation (13). It is evident that the measured temperature, T_m, differs significantly from the actual gas temperature, T_g, and that the measured temperature T_m, calculated by equation (13), is in good agreement with the experimental measurements (shown by symbols).

To understand the cause of this discrepancy, the OY-profiles of the gas temperature and the density of excited $\mathrm{N_2(C^3\Pi_u)}$ molecules were calculated at various time instants. The results are presented in figure 13 for $t = 3$ ns, 23 ns, and 28 ns. Although the maximum gas temperature increases with time, the overall shape of the temperature distribution along the OY axis changes insignificantly: for any time instant, the temperature peaks within $y \approx 0 - 30$ μm, with a maximum about 12.5 μm. In contrast to the temperature distribution, the OY-profiles of $\mathrm{N_2(C^3\Pi_u)}$ density vary significantly with time, becoming increasingly flattened in the region $y > 30$ μm. For example, at $t = 28$ ns, the calculated $\mathrm{N_2(C^3\Pi_u)}$ density, and consequently the SPS emission, extend into the region of a relatively cold gas (figure 13). As a result, the measured

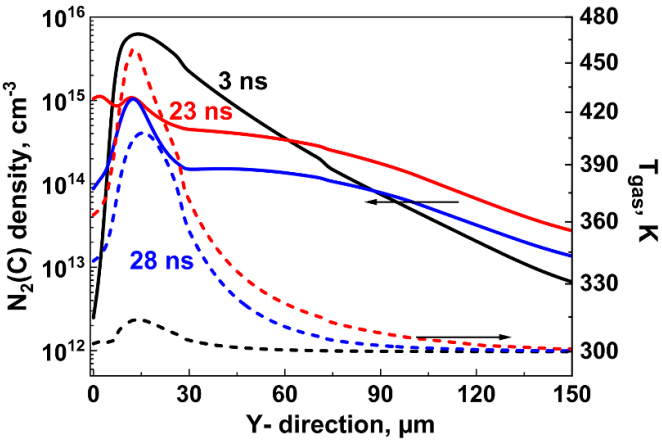

Figure 13. OY-profiles of $\mathrm{N_2(C^3\Pi_u)}$ and gas temperature in cross section $x = 1.0$ mm. Solid lines—$\mathrm{N_2(C^3\Pi_u)}$ density at $t = 3$ ns, 23 ns, 28 ns; dashed line—gas temperature at $t = 3$ ns, 23 ns, 28 ns.

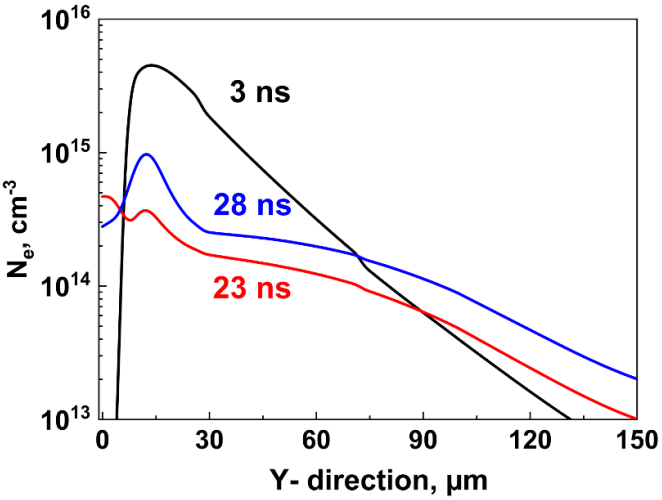

Figure 14. OY-profiles of electron density in cross section $x = 1.0$ mm at time instants $t = 3$ ns, 23 ns and 28 ns.

temperature T_m defined by the equation (13) is significantly lower than the actual gas temperature T_g.

To explain the observed 'flattening' of the OY-profiles of $\mathrm{N_2(C^3\Pi_u)}$, corresponding distributions of the electron density and of the electric field were calculated. Figure 14 shows the OY-profiles of electron density at time instants $t = 3$ ns, 23 ns, and 28 ns. Over time, the electron density profile (N_e) in the region $y > 30$ μm becomes more and more flat. The primary reason for this is the faster electron-ion recombination in regions with higher densities of charged particles. Finally, it is important to note that for $y > 10$ μm, the E/N distribution along the Y axis is relatively uniform. As a result, $[\mathrm{N_2(C^3\Pi_u)}]$ is approximately proportional to N_e, meaning that the $\mathrm{N_2(C^3\Pi_u)}$ profile closely follows the electron density profile.

It should be noted that similar OY–profiles of the electron density at the initial stage of discharge that were obtained in the numerical simulation of a surface DBD of positive polarity

in paper [33]. It was shown that the plasma is polarized by the electric field component normal to the dielectric surface. This polarization exists until the Y–component of the electric field inside the streamer channel reaches zero. As a result, a non-uniform OY–profile of the density of charged particles with a transverse size of 30 μm is formed with a maximum at a distance of 20–30 μm from the dielectric surface (see figure 6(c) of [33]). These results are consistent with the data obtained in our calculations and shown in figure 14 (see the curve corresponding to $t = 3$ ns).

Thus, in the SDBD under consideration, significantly different OY-profiles of gas temperature and $N_2(C^3\Pi_u)$ density can lead to substantial errors when measuring gas temperature using optical emission of the second positive system of nitrogen. The calculations presented in figure 12 clearly illustrate this point.

4.2.2. Discharge parameters in the second (probe) pulse. Analysis of SDBD parameters in the secondary (probe, or diagnostic) pulse, 500 ns after the main discharge, is of significant interest. The main distinguishing feature of the probe pulse is that it has a smaller amplitude and propagates through a gas that contains low-density regions. Indeed, according to the calculation results (see figure 13 and 2D map of the gas density in the appendix A), a heated layer is formed near the surface of the dielectric during the first pulse, specifically in the region of $y \approx$0–30 μm. The transverse dimension of this region is approximately 30 μm. The characteristic gas dynamic time (time of the gas pressure equalization for this area), is τ_g =60–70 ns. This indicates that at times $t \gg \tau_g$, the region of reduced gas density around $y = 12.5$ μm is formed. It is in this region that the main discharge energy is likely to be concentrated.

To analyse the SDBD parameters in the probe pulse, calculations were conducted for an additional, 'probe' pulse. 2D maps of the electron density and the reduced electric field at $t > 500$ ns are presented in appendix A. While the first pulse started at $t = 0$ ns and had the parameters shown in figure 9, the second, a probe pulse, occurred 500 ns later, with a lower gas density in the region mentioned above. The waveform of the second pulse was assumed to be similar to that of the first (as shown in figure 9) but with a lower amplitude of $U = +5$ kV.

Figure 15 presents the calculated reduced electric field and specific delivered energy at the point $(x; y) = (1$ mm; 25 μm) during the second pulse. The point corresponds to the maximum of gas temperature over the dielectric surface. Since the voltage amplitude of the second pulse is approximately one twentieth of the first, the specific energy input ω is significantly lower than in the first pulse. The E/N values in the second pulse are also lower than those in the first pulse (compare figures 10 and 15).

Kinetic curves of charged species and $N_2(C^3\Pi_u)$ density at a distance of 1 mm from the high-voltage electrode at 25 μm from the surface of the dielectric in the probe pulse are presented in figure 16. The curves are similar to those in the first main pulse but with lower absolute densities of the species. As in the first pulse (see figure 11 for comparison), the main positive ions during most of the discharge are O_2^+ and O_4^+,

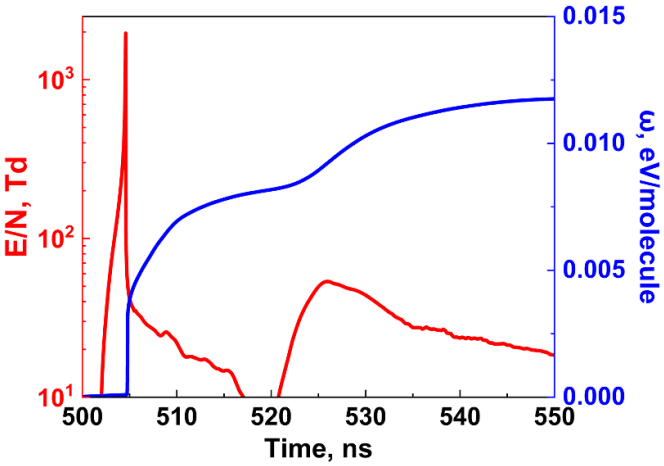

Figure 15. Temporal evolution of reduced electric field E/N and specific delivered energy ω at the point $(x; y) = (1$ mm; 25 μm) for the conditions of the probe pulse.

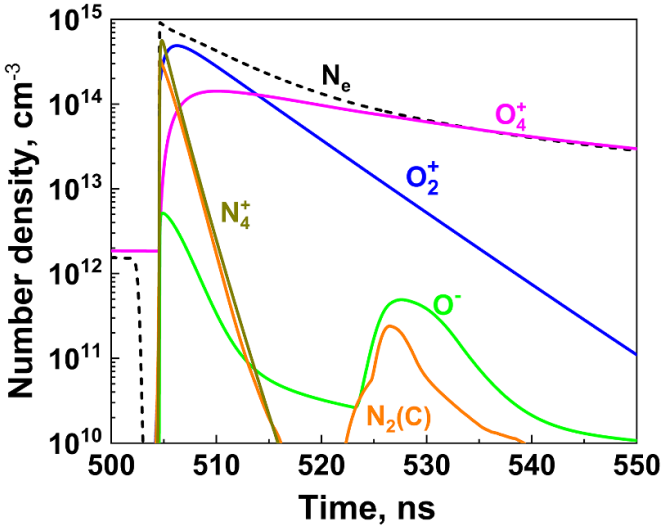

Figure 16. Time behaviour of the electron density, density of ions and $N_2(C^3\Pi_u)$ density at the point $(x; y) = (1$ mm; 25 μm) for the second (probe) pulse.

the role of negative ions is relatively small. The main differences are observed at times corresponding to the trailing edge of the voltage pulse. These differences are associated with the relatively low values of E/N in the probe pulse during the trailing edge of the voltage pulse (t =520–540 ns, see figure 15). As a consequence, no increase of electron density or densities of positive ions is observed at the trailing edge. The peak of $N_2(C^3\Pi_u)$ is still observed but much lower than on the rising front of the pulse, which means that if the ICCD imaging is integrated over the probe pulse, mainly the first peak is recorded.

A particularly interesting aspect is the comparison of the spatial distributions of gas temperature and SPS emission intensity during the second pulse. Figure 17 presents calculated OY-profiles of the gas temperature and density of excited $N_2(C^3\Pi_u)$ molecules at $x = 1$ mm for time instants $t = 506$ ns and 528 ns. As observed, a correlation exists between these

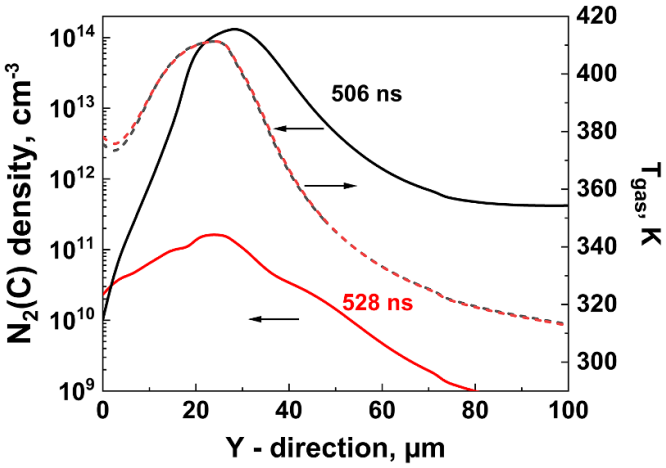

Figure 17. OY-profiles of $N_2(C^3\Pi_u)$ density and gas temperature in the cross section $x = 1.0$ mm. Solid lines—gas temperature; dashed lines—$N_2(C^3\Pi_u)$ density at $t = 506$ ns and 528 ns.

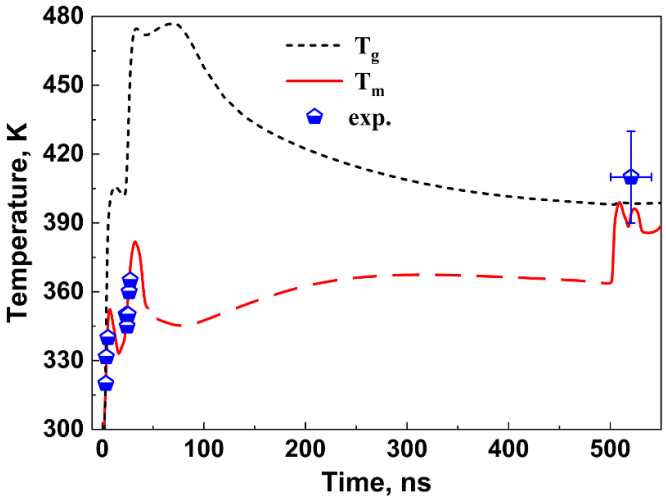

Figure 18. Temperature as a function of time in the main pulse and in the probe pulse 500 ns later: symbols are experimental data, curves are the results of calculations: short-dashed black curve represents calculated gas temperature $T_g(t)$ at the point $(x; y) =$ (1 mm; 12.5 μm), solid and long-dashed red curve provides $T_m(t)$ calculated by equation (13) (see text) at $x = 1$ mm.

distributions in the second pulse: the region of maximum values of $N_2(C^3\Pi_u)$ density and the region of high values of gas temperature are approximately the same, OY$= 20 -$ 40 μm. Consequently, the gas temperature in the second pulse, determined using the distribution of emission over rotational levels of the second positive system of nitrogen [22], should provide an accurate representation of the corresponding gas heating. This is in stark contrast to the first pulse, where the spatial distributions of gas temperature and SPS emission differed significantly (see figure 13).

4.2.3. Temperature over the main and probe pulses: calculations vs measurements. Let us consider the dynamics of the gas temperature at the point $(x; y) =$ (1 mm; 12.5 μm) together for the first pulse and for the probe pulse (black short-dashed curve in figure 18). The maximum heating of the gas at this point is achieved at times $t =$30–70 ns and the gas heating is equal to $\Delta T_g = 185$ K. This corresponds to the energy efficiency of FGH $\eta_R = 10\%$. Main processes responsible for the FGH mechanism during the discharge are the quenching of the $N_2(a^1\Pi_g, B^3\Pi_g, C^3\Pi_u)$ states by oxygen molecules and the quenching of excited $O(^1D)$ atoms by nitrogen molecules. Heating of the gas after the discharge pulse at atmospheric pressure is associated with the quenching of the $N_2(A^3\Sigma_u^+)$ states by oxygen molecules, with a characteristic time of 100 ns. It should be noted that the gas temperature drops relatively quickly at times $t > 100$ ns, which is explained by the gas-dynamic expansion of the hot region. This fast cooling is explained by the relatively small size of the heated gas region, $\Delta = 15 - 20$ μm (see figure 13). The minimal additional increase in gas temperature, a few degrees, occurs at $t > 500$ ns due to the small specific energy contribution in the second diagnostic pulse.

The solid and long-dashed red curve in figure 18 describes the time behavior of the expected to be measured gas temperature $T_m(t)$ at $x = 1$ mm, provided by the equation (13) and taking into account the calculated OY-distribution of the density of the emitting state. Experimental data, obtained by integration of the SPS emission over depth of field, are presented by symbols.

The calculated T_m for the second (probe) pulse is lower than the experimentally measured temperature, even if the increase of T_m in the second pulse is qualitatively reproduced. This difference can be due to the fact that the calculated data are obtained within the 2D-approximation, while in the experiment the system of plasma channels is 3-dimensional (see figure 5). As a consequence, the specific energy contribution in the experiment, and so the gas heating in the channels can exceed the calculated T_m values.

Summarizing the discussion above, it is possible to conclude that the low-energy probe pulse should be used for temperature measurement by optical emission spectroscopy in the afterglow of nanosecond SDBD. Additional control of the discharge emission pattern is recommended to assure that no strong changes in the discharge morphology are observed.

The gas temperature measured from the SPS emission in the probe pulse hundreds of nanoseconds after the main pulse approximately corresponds to the real gas temperature in the region of maximum heating. The reason for this is that the probe discharge is mainly concentrated in the region of lower gas density (in the zone of high E/N values); as a result, the main SPS emission comes exactly from the region in which the maximum gas heating in the first pulse took place.

Finally, will consider the time interval between the main pulse and the probe pulse, $30 < t < 500$ ns. During this period, gas-dynamic expansion with a characteristic timescale τ_g results in the cooling of the plasma channel heated by the first pulse (see black dashed curve in figure 18). To account for this difference and to determine the value of a possible maximum

value of gas heating T_{max} by the discharge, the following equation [54] can be used:

$$\frac{T_{expans}\,(t \gg \tau_g)}{T_0} = \left(\frac{P_{max}}{P_0}\right)^{1/\gamma} = \left(\frac{T_{max}}{T_0}\right)^{1/\gamma}, \qquad (14)$$

where γ is the heat capacity ratio, T_0 and P_0 are the values of gas temperature and pressure at the initial moment, T_{expans} is the gas temperature measured after the expansion of the channel and reaching the initial pressure $P = P_0$. Equation (14) is obtained under the assumption that the expansion of the hot channel is adiabatic ($P \sim \rho^{\gamma}$), and the main heating of the gas occurs at times t_{heat} much shorter than the gas-dynamic time ($t_{heat} \ll \tau_g$).

5. Conclusions

This paper presents the results of experimental and theoretical studies on the parameters of a nanosecond surface dielectric barrier discharge (SDBD) of positive polarity ($U = +27.5$ kV on the high-voltage electrode) in atmospheric-pressure air, with a pulse duration of 20 ns. The study includes measurements of the discharge current, delivered energy, and discharge morphology using ICCD imaging, as well as gas heating both in the discharge and in a probe pulse occurring 500 ns after the initial main pulse.

The results of 2D numerical modeling of nanosecond SDBD are presented. The calculations are performed using the model described and tested in detail in [25, 26], [40, 41]. The calculation results are compared with experimental data on the discharge current, total delivered energy and temperature.

Calculations show that the main energy deposition into the gas does not occur at the peak electric fields (E/N =1000–3000 Td) in the ionization front, but rather during their subsequent decline to moderate values (E/N =70–170 Td) at the leading edge of the voltage pulse and under similar moderate fields at the trailing edge. The fact that the major part of energy is deposited under relatively low-field conditions explains why the fraction of energy spent on fast gas heating (FGH) during the discharge pulse does not exceed $\eta_R = 10\%$.

It is shown that, in the main discharge pulse, there is a significant difference between the OY-profiles (normal to the dielectric surface) of gas temperature and the emission intensity of 2^+ system of molecular nitrogen. As a result, measurements of the gas temperature based on the 2^+ emission during the falling edge of the pulse can lead to significant errors. The reason for the difference of these profiles is that the spatial distribution of gas heating is formed at the first nanoseconds and changes weakly with time, while the emission intensity profile follows the electron density distribution, which becomes flatter with time due to the electron-ion recombination. A significant contribution to the total intensity of 2^+ system of nitrogen is made by the emission from regions with a relatively low gas temperature.

Calculations of SDBD parameters are also carried out in a second (probe) pulse of smaller amplitude 500 ns after the first discharge pulse. The main distinguishing feature of the probe pulse is that it propagates through the gas containing regions of smaller gas density. As a result, the OY-profiles of gas heating and intensity of the nitrogen 2^+ system are similar. As a result, the temperature can be measured correctly on the basis of the SPS emission under conditions that no strong changes in the discharge morphology leading to additional heat are observed.

It should be noted that during the time interval between the main and probe pulses, a noticeable cooling of the hot channel occurs, which is associated with its gas-dynamic expansion. Therefore, the gas temperature measured at times $t \gg \tau_g$ will differ from the temperature T_{max} at the end of the main discharge pulse.

The conclusions above may apply not only to SDBD but also to volumetric nanosecond discharges. It is worth noting that an alternative temperature measurement technique, such as Spontaneous Raman scattering [12, 55] or CARS [53], can be used to determine gas heating in the discharge afterglow—however, these methods are more complex than emission spectroscopy of rotational manifold of the second positive system of molecular nitrogen.

Data availability statement

All data that support the findings of this study are included within the article (and any supplementary files).

Acknowledgments

Work of G Kreyder and S M Starikovskaia was partially supported by Agence de l'Innovation de Défense—AID—via Centre Interdisciplinaire d'Etudes pour la Défense et la Sécurité—CIEDS - (project 2022 - PPRINCE), Cellule Énergie du CNRS (PEPS 2024 Project ZEPhiR) and Energy4Climate Interdisciplinary Center (E4C) of IP Paris and Ecole des Ponts ParisTech in the framework of the 3rd Programme d'Investissements d'Avenir [ANR-18-EUR-0006-02]. Work of N.A.Popov was supported by Russian Science Foundation, Project No. 23-17-00264. The authors are thankful to Prof. Yifei Zhu for possibility to use his PASSKEy code and for numerous discussions.

Author contributions

Bin Zhang
Formal analysis (equal), Investigation (equal), Software (lead), Validation (equal), Writing – original draft (equal)

Nikolay Popov 0000-0001-8738-9642
Data curation (equal), Resources (equal), Validation (equal), Visualization (equal)

Sergey A Shcherbanev
Conceptualization (lead), Formal analysis (equal), Investigation (equal), Validation (equal), Writing – original draft (equal)

Appendix A

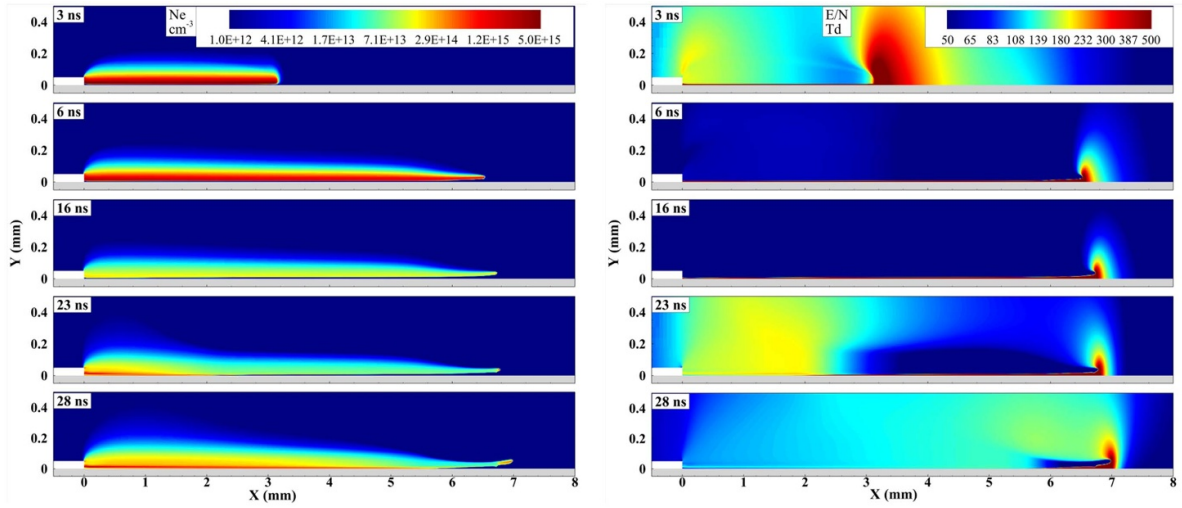

Figure 19. Calculated evolution of the electron density (left) and reduced electric field (right) during the main pulse. Time instants are marked within each frame.

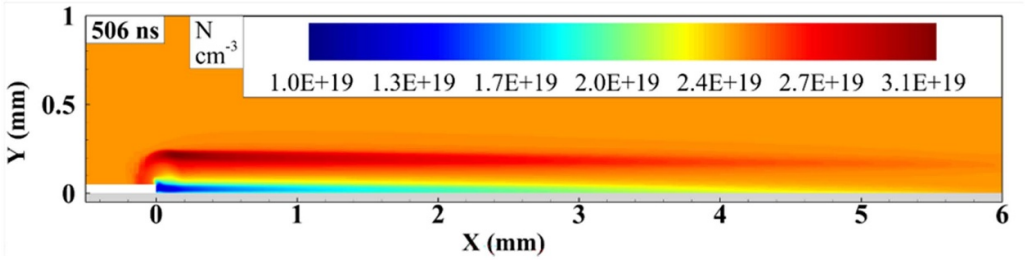

Figure 20. Calculated neutral gas density at 506 ns.

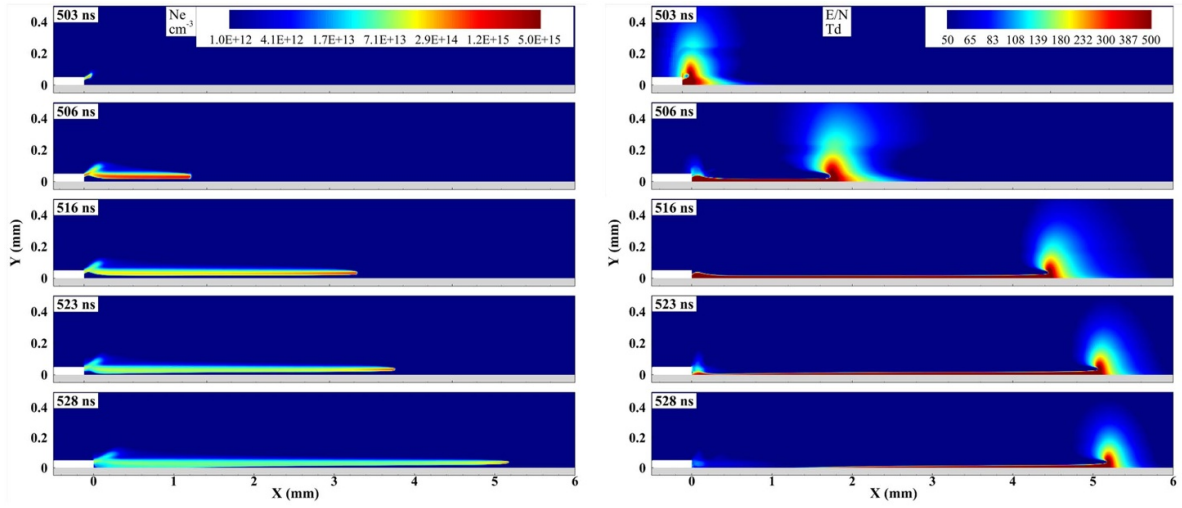

Figure 21. Calculated evolution of the electron density (left) and reduced electric field (right) during the main pulse. Time instants are marked within each frame.

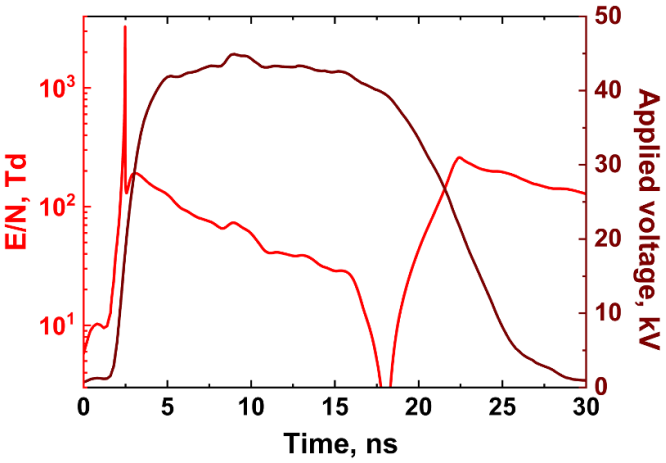

Figure 22. Temporal evolution of measured applied voltage at the HV electrode and calculated reduced electric field E/N at the point $(x; y) = (1\text{ mm}; 12.5\ \mu\text{m})$ for the conditions of [23, 24].

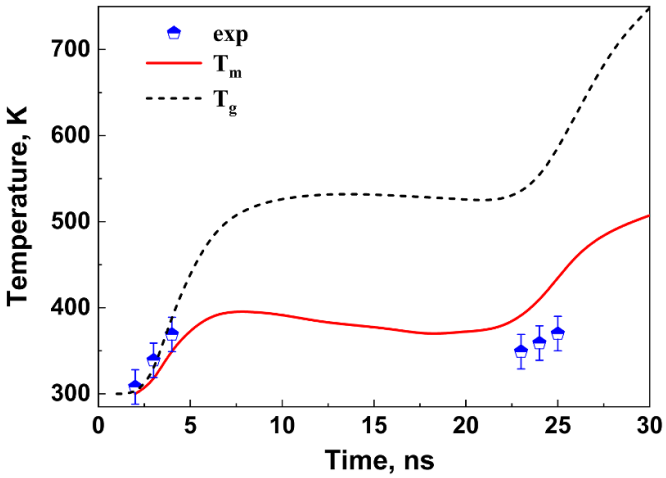

Figure 23. Temperature as a function of time in SDBD under the conditions of [23, 24]: symbols are experimental data [24], curves are the results of calculations: dashed curve represents calculated gas temperature $T_g(t)$ at the point $(x; y) = (1\text{ mm}; 12.5\ \mu\text{m})$, solid curve provides $T_m(t)$ calculated by equation (13) at $x = 1$ mm.

Appendix B

To test the model suggested in the paper, the SDBD parameters were calculated for conditions corresponding to the experiments [23, 24]. The discharge was studied in air at atmospheric pressure at positive polarity pulse, duration at FWHM of 20 ns, and a voltage amplitude $U = +45$ kV. Differently from the present work (see figure 1), the length of the grounded electrode was much longer, $|\text{DE}| = 50$ mm. The waveform of voltage on the HV electrode used in the calculations is shown in figure 22.

Temporal evolution of the measured applied voltage and absolute value of the calculated reduced electric field E/N at the point $(x; y) = (1\text{ mm}; 12.5\ \mu\text{m})$ are presented in figure 22. Despite the high electric fields at the head of the surface streamer, where E/N reaches 3000 Td, the majority of the discharge energy is deposited in the gas at reduced electric fields of $E/N = 60$–170 Td.

In [23, 24], similar to the present work, the optical emission of 2^+ system of nitrogen was used to measure gas temperature in nanosecond SDBD. The spectra were obtained over the region 0–2 mm counting from the HV electrode with the ICCD camera gate equal to 1 ns. Figure 23 shows the results of the comparison of the calculated and experimental time profiles of gas temperature, the points are experimental data [24]], and the curves are the calculation results: T_g is the gas temperature at the point $(x; y) = (1\text{ mm}; 12.5\ \mu\text{m})$; T_m is the expected to be measured temperature over the depth of field at $x = 1$ mm, provided by equation (13) of the present work (see [15] for details).

As observed, the calculated temperature waveform expected to be measured, T_m, shows a reasonable agreement with the measured data (points), indicating that the developed model adequately describes the gas temperature increase and takes into account peculiarities of measurements. The overall time evolution of the gas temperature follows a similar pattern to that shown earlier in figure 12: a rapid temperature increase occurs within the first 3–4 ns, during the leading edge of the voltage pulse, followed by the next temperature rise at the trailing edge of the pulse. Will note that a significant discrepancy is observed between measured T_m and calculated T_g: for example, at the end of the discharge pulse, at $t = 25$ ns, the temperature difference $\Delta T = T_g$—T_m reaches 150 K. As in the case discussed in the section 4.2.1, this difference comes from the difference in the OY profiles of the gas temperature and the SPS emission intensity.

References

[1] Roth J, Sherman D and Wilkinson S 2000 Electrohydrodynamic flow control with a glow-discharge surface plasma *AIAA J.* **38** 1166–72
[2] Roth J 2003 Aerodynamic flow acceleration using paraelectric and peristaltic electrohydrodynamic effects of a one atmosphere uniform glow discharge plasma *Phys. Plasmas* **10** 2117–26
[3] Enloe C, McLaughlin T, VanDyken R, Kachner K, Jumper E, Corke T, Post M and Haddad O 2004 Mechanisms and responses of a single dielectric barrier plasma actuator: geometric effects *AIAA J.* **42** 595–604
[4] Enloe C, McHarg M and McLaughlin T 2008 Time correlated force production measurements of the dielectric barrier discharge plasma aerodynamic actuator *J. Appl. Phys.* **103** 073302
[5] Brandenburg R 2017 Dielectric barrier discharges: progress on plasma sources and on the understanding of regimes and single filaments *Plasma Sources Sci. Technol.* **26** 053001
[6] Starikovskii A Y, Nikipelov A, Nudnova M and Roupassov D 2009 SDBD plasma actuator with nanosecond pulse-periodic discharge *Plasma Sources Sci. Technol.* **18** 034015
[7] Leonov S, Adamovich I and Soloviev V 2016 Dynamics of near-surface electric discharges and mechanisms of their interaction with the airflow *Plasma Sources Sci. Technol.* **25** 063001
[8] Starikovskiy A Y and Aleksandrov N L 2021 Gasdynamic flow control by ultrafast local heating in a strongly nonequilibrium pulsed plasma *Plasma Phys. Rep.* **47** 148–209

[9] Popov N and Starikovskaia S 2022 Relaxation of electronic excitation in nitrogen/oxygen and fuel/air mixtures: fast gas heating in plasma-assisted ignition and flame stabilization *Prog. Energy Combust. Sci.* **91** 100928
[10] Rusterholtz D, Lacoste D, Stancu G, Pai D and Laux C 2013 Ultrafast heating and oxygen dissociation in atmospheric pressure air by nanosecond repetitively pulsed discharges *J. Phys. D: Appl. Phys.* **46** 464010
[11] Ono R, Teramoto Y and Oda T 2010 Gas density in a pulsed positive streamer measured using laser shadowgraph *J. Phys. D: Appl. Phys.* **43** 345203
[12] Lo A, Cessou A, Boubert P and Vervisch P 2014 Space and time analysis of the nanosecond scale discharges in atmospheric pressure air: I. Gas temperature and vibrational distribution function of N_2 and O_2 *J. Phys. D: Appl. Phys.* **47** 115201
[13] Brisset A, Guichard F, Cessou A and Tardiveau P 2021 Energy relaxation and heating in the afterglow of high electric field ns-discharges in ambient air using spontaneous Raman scattering *Plasma Sources Sci. Technol.* **30** 035013
[14] Montello A, Burnette D, Nishihara M, Lempert W R and Adamovich I V 2013 Dynamics of rapid localized heating in nanosecond pulse discharges for high speed flow control *J. Fluid Sci. Technol* **8** 147–59
[15] Lepikhin N, Popov N and Starikovskaia S 2018 Fast gas heating and radial distribution of active species in nanosecond capillary discharge in pure nitrogen and N_2:O_2 mixtures *Plasma Sources Sci. Technol.* **27** 055005
[16] Mintoussov E I, Pendleton S J, Gerbault F G, Popov N A and Starikovskaia S M 2011 Fast gas heating in nitrogen-oxygen discharge plasma: II. Energy exchange in the afterglow of ame nanosecond discharge at moderate pressures *J. Phys. D: Appl. Phys.* **44** 285202
[17] Popov N A 2016 Pulsed nanosecond discharge in air at high specific deposited energy: fast gas heating and active particles production *Plasma Sources Sci. Technol.* **25** 044003
[18] Aleksandrov N L, Kindysheva S V, Nudnova M M and Starikovskiy A Y 2010 Mechanism of ultra-fast heating in a non-equilibrium weakly ionized air discharge plasma in high electric fields *J. Phys. D: Appl. Phys.* **43** 255201
[19] Nudnova M M, Aleksandrov N L and Starikovskiy A Y 2010 Influence of theage polarity on the properties of a nanosecond surface barrier discharge in atmospheric-pressure air *Plasma Phys. Rep.* **36** 90–98
[20] Nudnova M M, Kindysheva S V, Aleksandrov N L and Starikovskii A Y 2015 Fast gas heating in N_2/O_2 mixtures under nanosecond surface dielectric barrier discharge: the effects of gas pressure and composition *Phil. Trans. R. Soc. A* **373** 20140330
[21] Bruggeman P J, Sadeghi N, Schram D C and Linss V 2014 Gas temperature determination from rotational lines in non-equilibrium plasmas: a review *Plasma Sources Sci. Technol.* **23** 023001
[22] Laux C O, Spence T G, Kruger C H and Zare R N 2003 Optical diagnostics of atmospheric pressure air plasmas *Plasma Sources Sci. Technol.* **12** 125
[23] Shcherbanev S A, Stepanyan S A, Popov N A and Starikovskaia S M 2015 Dielectric barrier discharge for multipoint plasma-assisted ignition at high pressures *Phil. Trans. R. Soc. A* **373** 20140342
[24] Shcherbanev S 2016 Filamentary nanosecond surface dielectric barrier discharge at elevated pressures: Streamer-to-filamentary transition and application for plasma-assisted combustion *PhD Thesis* Université Paris-Saclay
[25] Zhu Y and Starikovskaia S M 2018 Fast gas heating of nanosecond pulsed surface dielectric barrier discharge: spatial distribution and fractional contribution from kinetics *Plasma Sources Sci. Technol.* **27** 124007
[26] Zhu Y, Shcherbanev S, Baron B and Starikovskaia S 2017 Nanosecond surface dielectric barrier discharge in atmospheric pressure air: I. Measurements and 2D modeling of morphology, propagation and hydrodynamic perturbations *Plasma Sources Sci. Technol.* **26** 125004
[27] Zhang Y, Guo Y, Zhu Y and Sun A 2025 Inhibition and promotion of quasi-uniform to filamentary discharge transition in negative repetitive nanosecond surface dielectric barrier discharge *Plasma Sources Sci. Technol* submitted (https://doi.org/10.48550/arXiv.2502.03923)
[28] Anikin N, Pancheshnyi S, Starikovskaia S and Starikovskii A Y 1998 Breakdown development at high overvoltage: electric field, electronic level excitation and electron density *J. Phys. D: Appl. Phys.* **31** 826
[29] Pavan C A, Rao S R and Guerra-Garcia C 2024 Tutorial: electrical measurements in nanosecond pulsed plasma reactors *J. Phys. D: Appl. Phys.* **58** 032502
[30] Khomenko A, Podolsky V and Wang X 2021 Different approaches of measuring high-voltage nanosecond pulses and power delivery in plasma systems *Electr. Eng.* **103** 57–66
[31] Lepikhin N D, Popov N A and Starikovskaia S M 2022 On electric field measurements based on intensity ratio of 1^- and 2^+ systems of nitrogen in discharges with high specific deposited energy *Plasma Sources Sci. Technol.* **31** 084002
[32] Pancheshnyi S, Starikovskaia S and Starikovskii A 2000 Collisional deactivation of $N_2(C\,^3\pi_u, v = 0, 1, 2, 3)$ states by N_2, O_2, H_2 and H_2O molecules *Chem. Phys.* **262** 349–57
[33] Soloviev V R and Krivtsov V M 2018 Numerical modelling of nanosecond surface dielectric barrier discharge evolution in atmospheric air *Plasma Sources Sci. Technol.* **27** 114001
[34] Soloviev V R, Anokhin E M and Aleksandrov N L 2020 Spatial distribution of radiation emitted by pulsed surface dielectric barrier discharge in air *Plasma Sources Sci. Technol.* **29** 035006
[35] Chen X, Zhu Y, Wu Y, Hao J, Ma X and Lu P 2021 Numerical investigations of nanosecond surface streamers at elevated pressure *Plasma Sources Sci. Technol.* **30** 075008
[36] Peng B, Jiang N, Zhu Y, Li J and Wu Y 2024 Three-electrode surface dielectric barrier discharge driven by repetitive pulses: streamer dynamic evolution and discharge mode transition *Plasma Sources Sci. Technol.* **33** 045018
[37] Zhang B, Zhu Y, Zhang X, Popov N, Orriere T, Pai D Z and Starikovskaia S M 2023 Streamer-to-filament transition in pulsed nanosecond atmospheric pressure discharge: 2D numerical modeling *Plasma Sources Sci. Technol.* **32** 115014
[38] Chen X, Zhu Y and Wu Y 2020 Modeling of streamer-to-spark transitions in the first pulse and the post discharge stage *Plasma Sources Sci. Technol.* **29** 095006
[39] Chen X, Zhu Y, Wu Y, Hao J, Ma X and Lu P 2021 Modeling of fast ionization waves in pure nitrogen at moderate pressure *Plasma Sources Sci. Technol.* **30** 065002
[40] Li Y, Guo Y, Zhu Y and Sun A 2023 A computational study of pseudo-filamentary nanosecond pulsed dielectric barrier discharge in atmospheric air *Phys. Plasmas* **30** 033509
[41] Li M, Chen S, Zhu Y, Li Y, Wang F, Cui Y and Zhuang C 2023 Experimental and numerical investigation of surface streamers in a nanosecond pulsed packed bed reactor *Plasma Sources Sci. Technol.* **32** 065002
[42] Ma X, Bai L, Zhu Y, Jiang X and Wu Y 2024 Numerical investigation of discharge evolution and breakdown characteristics of ArF excimer lasers *Plasma Sources Sci. Technol.* **33** 075012
[43] Li J, Jiang N, Wang X, Yu G, Peng B, He J and Li J 2024 Streamer propagation characteristics of nanosecond pulsed discharge plasma on fluidized particles surface:

experimental investigation and numerical simulation *J. Phys. D: Appl. Phys.* **57** 255203
[44] Zhu Y, Wu Y, Wei B, Xu H, Liang H, Jia M, Song H and Li Y 2019 Nanosecond-pulsed dielectric barrier discharge-based plasma-assisted anti-icing: modeling and mechanism analysis *J. Phys. D: Appl. Phys.* **53** 145205
[45] Zhu Y, Chen X, Wu Y, Hao J, Ma X, Lu P and Tardiveau P 2021 Simulation of ionization-wave discharges: a direct comparison between the fluid model and e-fish measurements *Plasma Sources Sci. Technol.* **30** 075025
[46] Hagelaar G J M and Pitchford L C 2005 Solving the Boltzmann equation to obtain electron transport coefficients and rate coefficients for fluid models *Plasma Sources Sci. Technol.* **14** 722–33
[47] Rethmel C, Little J, Takashima K, Sinha A, Adamovich I and Samimy M 2011 Flow separation control using nanosecond pulse driven dbd plasma actuators *Int. J. Flow Control* **3** 213–32
[48] Babaeva N Y, Tereshonok D V and Naidis G V 2016 Fluid and hybrid modeling of nanosecond surface discharges: effect of polarity and secondary electron emission *Plasma Sources Sci. Technol.* **25** 044008
[49] Cao Y S and Johnsen R 1991 Recombination of n_4^+ ions with electrons *J. Chem. Phys.* **95** 7356–9
[50] Klopovsky K S, Mukhovatova A V, Popov A M, Popov N A, Popovicheva O B and Rakhimova T V 1994 Kinetics of metastable states in high-pressure nitrogen plasma pumped by high-current electron beam *J. Phys. D: Appl. Phys.* **27** 1399–405
[51] Tibere-Inglesse A C, McGuire S D and Laux C O 2023 Inferring gas temperature from N_2 emission via rotational distribution of the N2 $B^3\Pi_g$ and $C^3\Pi_u$ states *Plasma Sources Sci. Technol.* **32** 075018
[52] Parker J G 1959 Rotational and vibrational relaxation in diatomic gases *Phys. Fluids* **2** 449–62
[53] Montello A, Yin Z, Burnette D, Adamovich I and Lempert W 2013 Picosecond cars measurements of nitrogen vibrational loading and rotational/translational temperature in non-equilibrium discharges *J. Phys. D: Appl. Phys.* **46** 464002
[54] Askarian G A, Mkheidze G P and Savin A A 1984 Determining the distribution of the energy deposition from the pulsed shuddering of the medium and the decrease in the gas density during the passage of an intense relativistic electron beam *Sov. Tech. Phys. Lett.* **10** 1465–8
[55] Brisset A, Tardiveau P, Gazeli K, Bournonville B, Jeanney P, Ouaras K, Magne L and Pasquiers S 2021 Experimental study of the effect of water vapor on dynamics of a high electric field non-equilibrium diffuse discharge in air *J. Phys. D: Appl. Phys.* **54** 215204